Inverse Error Function Trajectories for Image Reconstruction*

Rohan Katoch¹, Beatriz Fusaro¹ and Jun Ueda¹

Abstract—Capturing clear images while a camera is moving fast, is integral to the development of mobile robots that can respond quickly and effectively to visual stimuli. This paper proposes to generate camera trajectories, with position and time constraints, that result in higher reconstructed image quality. The degradation in of an image captured during motion is known as motion blur. Three main methods exist for mitigating the effects of motion blur: (i) controlling optical parameters, (ii) controlling camera motion, and (iii) image reconstruction. Given control of a camera's motion, trajectories can be generated that result in an expected blur kernel or point-spread function. This work compares the motion blur effects and reconstructed image quality of three trajectories: (i) linear, (ii) polynomial, and (iii) inverse error. Where inverse error trajectories result in Gaussian blur kernels. Residence time analysis provides a basis for characterizing the motion blur effects of the trajectories.

I. INTRODUCTION

Visual information is a primary mode of knowledge-acquisition for robotic systems that function in unstructured environments (e.g. mobile robots). For these systems to intelligently react to and interact with the environment effectively, visual signals need to be processed at a high-level and in an efficient manner. The acquisition of high-quality signals from the environment is a fundamental problem that needs to be resolved. Currently, cameras have found prevalent use as they provide a rich source of information which is useful for resolving problems in a large number of areas (e.g. localization, object recognition, path planning) [1].

For systems in motion, the image captured by cameras gets degraded by motion blur. Since a finite exposure time is required for sufficient charge to develop in the photosensitive element, relative motion between a camera and a scene causes the sensor to capture information from different points in space.e. There are two sources of motion blur: (i) camera motion, and (ii) scene motion [2]. Motion of a camera relative to the scene being captured results in spatiallyinvariant (global) blur. All parts of an image captured under global blur are affected by the same type of motion. If the camera motion is known, it can be used to deblur the entire image. In contrast, scene motion relative to a camera can result in spatially-varying (local) blur. Mitigating local blur requires the application of spatially-varying filters. In this work stationary orthographic scenes with negligible changes in depth are considered, resulting only in global blur.

Many methods of mitigating motion blur have been considered by the computational imaging community. In general, these methods either involve controlling optical parameters of the camera (exposure, aperture, and focal length), controlling the motion of the camera, or image reconstruction through post-processing.

Generating good quality images with very short exposure times is possible through the use of high-speed cameras. Since significant motion is not allowed at the image capture timescale motion bur effects are negligible. Although, these cameras are expensive and lead to very high data rates that a robotic system would need to be capable of storing and processing. Other methods that involve active control of optical parameters include coded exposure (flutter shutter) [3], coded aperture [4], and focal sweep [5]. These methods use intelligently control optical parameters during image capture, followed by post-processing, to mitigate motion blur. The ability to actively control optical parameters is not present in most commercially available cameras. Furthermore, these methods generally require a stationary camera and are not applicable under the constraints of the problem considered in this paper.

Controlling the motion of the camera enables control over the point spread function (PSF), which describes how a single point of light is spread over the imaging sensor. For a stationary camera the PSF would ideally be a point of the same width as the light beam, however aberrations due to optical elements always exist. Given knowledge of how an imaging system will move, feed-forward control signals can be generated to compensate the motion and stabilize the imaging sensor. If computed and executed exactly, the image will be generated as if the imaging system is stationary. However, this method is limited by the speed and range of the compensating mechanism.

Image reconstruction aims to solve the inverse problem of generating a latent image from an image degraded by motion blur, through the use of prior knowledge (e.g. motion information, natural image statistics) [6], [7], [8], [9]. Reconstruction is typically performed by first estimating the point-spread function (PSF), and then performing deconvolution.

The focus of this work is path planning for imaging systems in fast motion, with the objective of capturing good quality images. By controlling the camera trajectory, the resulting PSF can also be controlled. Knowledge of the expected PSF can then be used for image reconstruction. Similar approaches have been considered in literature, but not in the same context. Levin et al. [10], propose moving an imaging device in parabolic trajectories during exposure. This results in PSFs that are invariant to blur

^{*}This material is based upon work supported by the National Science Foundation under Grant No. 1662029

¹ Bio-Robotics and Human Modeling Lab, George W. Woodruff School of Mechanical Engineering, Georgia Institute of Technology, Atlanta, GA 30332 USA rkatoch3@gatech.edu

effects caused by objects moving at constant velocity in a particular direction. This method was further extended by Cho et al. [11] to include all planar motion directions by taking orthogonal exposures. However, it is impractical to take multiple exposures of the same scene. Bando et al. [12] propose circular trajectories which generate kernels that are orientation invariant for linear motion.

In contrast to past approaches, the approach proposed in this paper focuses on trajectories that reduce the effects of motion blur under time and position constraints. Trajectories based on the inverse error function are shown to generate deblurred images with lower mean squared error (MSE), when compared to linear and parabolic trajectories. Furthermore, since inverse error trajectories result in Gaussian PSFs the reconstructed image is robust to additive noise. Within this family of trajectories, a variance parameter needs to be selected which has implications on the final time and reconstructed image quality. The main point of interest in this study, is to examine how receding the time horizon affects the trajectories generated and therefore the resulting blurry image. Residence time analysis provides a basis for trajectory generation.

II. MATHEMATICAL FORMULATION OF MOTION DEBLURRING

A. Problem Statement

Consider an imaging device that is in motion within a planar space $\mathscr{X}\subseteq\mathbb{R}^2$, with position $\mathbf{x}=(x,y)\in\mathscr{X}$, nonlinear state dynamics $f(\mathbf{x})$, mass m and control u. There are two objectives to accomplish: (i) reach final position \mathbf{x}_f at t_f , and (ii) capture image $I(\mathbf{x}_\epsilon)$. A one-dimensional schematic of the problem and sample trajectory is presented in Figures 1 and 2 respectively. For convenience, a sample trajectory which is symmetric about x_ϵ and stationary at x_ϵ is considered without a loss of generality. The exposure window $T_\epsilon = (t_\epsilon, t_\epsilon + \tau]$, with duration τ , is the time period during which the camera sensor captures information. The trajectory parameters D and θ are defined by (1).

$$D = \frac{x_f - x_0 - 2\gamma}{2}, \quad \theta = \frac{t_f - t_0 - \tau}{2}$$
 (1)

Given initial and final positions (x_0,x_f) , initial time t_0 and exposure parameters (τ,γ) , the time horizon t_f defines the speed outside of the exposure window. Based on continuity, this speed is considered the initial speed during the exposure window $\dot{x}(x^-)$ and will be known as the entry speed v_e .

B. Image Formation

The photon-capture process used for camera sensors is affected by two main sources of noise: (i) shot noise, and (ii) Johnson-Nyquist (thermal) noise [13]. Shot noise is the result of variance in the number of photons captured by photo-sensitive elements over time, and is proportional to the square-root of the light intensity on a per-pixel basis [14]. The per-pixel dependence is dropped and the variance is approximated to be proportional to the square-root of

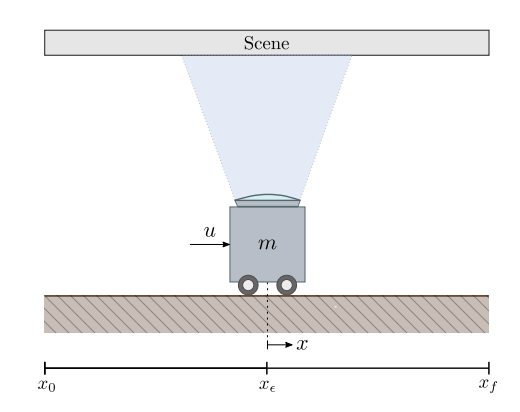


Fig. 1. Schematic of imaging device in controlled motion.

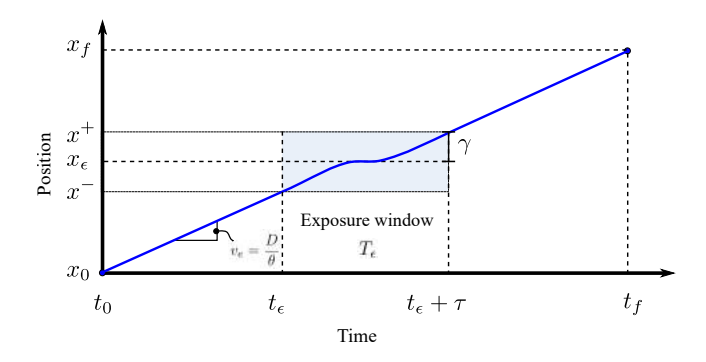


Fig. 2. Example of trajectory for imaging device in controlled motion.

average light intensity, denoted by λ . Thermal noise refers to the electrical noise caused by thermal agitation of electrons within the imaging sensor.

Shot noise is modeled as a stationary Poisson process \mathscr{P} with intensity λ , and thermal noise is modeled as an additive zero-mean Gaussian process \mathscr{N} with variance σ^2 . Both processes are independent and their increments are stationary. The Poisson process generates a blurry image B to which Gaussian noise N is added, resulting in captured image I. Therefore, for latent image L at exposure position \mathbf{x}_{ϵ} and exposure period T_{ϵ} , the captured image is described by (2) and (3).

$$B \sim \mathscr{P}\left(\lambda \int_{T_{\epsilon}} L(\mathbf{x}(t)) dt\right), \quad N \sim \mathscr{N}\left(0, \sigma^{2}\right) \quad (2)$$

$$I(\mathbf{x}_{\epsilon}) = B(\mathbf{x}_{\epsilon}; \lambda, \mathbf{x}(t), T_{\epsilon}) + N(\mathbf{x}_{\epsilon})$$
(3)

The exposure position \mathbf{x}_{ϵ} is defined to be the average position for the trajectory $\mathbf{x}(t)$ during the exposure window T_{ϵ} .

$$\mathbf{x}_{\epsilon} = \frac{1}{\tau} \int_{T_{\epsilon}} \mathbf{x}(t) dt \tag{4}$$

A sample image I^* can be generated by evaluating the expectation $\mathbb E$ and variance $\mathbb V$ of the image model, as in (5)

– (7). Where, $\alpha \sim \mathcal{N}(0,1)$ is a normally distributed random variable. When $|\alpha| = 1$, the effects of noise are greatest.

$$I^* = \mathbb{E}[B] + \alpha \sqrt{\mathbb{V}[B] + \mathbb{V}[N]}$$
 (5)

$$\mathbb{E}[B] = \mathbb{V}[B] = \lambda \tau \int_{T_{\epsilon}} L(\mathbf{x}(t)) dt$$
 (6)

$$V[N] = \sigma^2 \tag{7}$$

C. Image Reconstruction

Reconstructed image $\hat{L}(\mathbf{x}_{\epsilon})$ is generated by deconvolution with expected PSF \hat{K} . The real kernel K is assumed to accurately represent the time-dependent process which generates motion blur. This assumption holds true when considering global blur. The image model in (3) can now be expressed using the convolution operator \otimes , as shown in (8).

$$I(\mathbf{x}_{\epsilon}) = K(\mathbf{x}(t)) \otimes L(\mathbf{x}_{\epsilon}) + N(\mathbf{x}_{\epsilon})$$
(8)

Prior work by the authors [15] has shown that motion information can be utilized for direct estimation of PSFs. This process is known as dynamics-based motion deblurring and enables real-time deblurring and panoramic generation [16]. After PSF estimation, a deconvolution process is used to generate the reconstructed image. The Richardson-Lucy deconvolution algorithm provides a Bayesian-based iterative procedure which is robust against noise [17], [18].

III. RESIDENCE TIME ANALYSIS

The following analysis will be done for a one-dimensional state $x \in \mathbb{R}$ for ease of representation, but can be extended for the planar case.

For a trajectory x(t) over exposure period T_{ϵ} , residence time is defined as the amount of time spent at a certain position during the exposure period. That is, it is described by the mapping $\tau_r(x): \mathbb{R} \to \mathbb{R}^+$ which will be called a residence time distribution (RTD). In the case of a stationary camera at position x_{ϵ} , the RTD is a delta function located at x_{ϵ} with value τ . For monotonically increasing trajectories x(t), when $\dot{x} \neq 0 \ \forall t \in T_{\epsilon}$, the expression for $\tau_r(x)$ can be found using (9).

$$\tau_r(x) = \frac{1}{\dot{x}(x)} \tag{9}$$

For a given RTD, a monotonically increasing solution is unique and also provides a lower bound on the speed at a given position. If the system moves faster than the bound at a certain position, then it must be revisited until the sum of the residence times equal the value defined by the distribution.

Getting a closed form solution for monotonically increasing trajectories is not feasible, as it would require a general solution to all possible first-order ordinary differential equations (ODEs). However, the relation above can be used to analytically construct a RTD. For the purposes of image reconstruction, the RTD is useful due to its proportionality with the expected PSF. Given this fact, several desirable

characteristics for the residence time distribution are determined: (i) maximal at x_{ϵ} , (ii) symmetric about x_{ϵ} , and (iii) constrained support.

Given that the objective is reconstruction of latent image $L(x_\epsilon)$, being located at x_ϵ for the maximum amount of time during exposure is ideal. The global maximum for an RTD should therefore be located at x_ϵ . Local maxima exist where $\dot{x}=0$, or where speed is minimum over the trajectory. The residence time values at a local maximum where $\dot{x}=0$ can be determined as the length of time the system is stationary at that position. Therefore, multiple stationary points can exist but the longest stationary point should be x_ϵ . If no stationary points exist, then the minimum speed should occur at x_ϵ .

Symmetric distributions ensure that an equivalent amount of information is distributed around the exposure position x_{ϵ} . If the distribution is skewed, this implies that the trajectory is faster on one side of x_{ϵ} than the other. Moving through space at different speeds leads to a change in the power spectra of the image [10]. This is not desirable, and therefore points equidistant from x_{ϵ} should have the same speed. Therefore the trajectory must pass through x_{ϵ} when $t = t_{\epsilon} + \tau/2$.

The compact support of the distribution is determined by the minimum x^- and maximum x^+ position values of the trajectory during exposure. For monotonically increasing trajectories, the minimum and maximum values are the positions at the beginning and end of exposure. For image reconstruction, these bounds determine the blur kernel size.

While the analysis has been restricted to monotonically increasing functions, monotonically decreasing functions can be treated similarly. Furthermore, these trajectories can be composed periodically to generate more complex trajectories. Distribution shape does not change under periodic composition, but distribution mass increases in proportion with the number of periods.

$$\int_{x^{-}}^{x^{+}} \tau_r(x) \mathrm{d}x = \tau \tag{10}$$

Given the constraints defined above, there are still a number of possible trajectories and no clear basis for a choice. We observe the fact that for a given exposure duration, the mass of a distribution must remain unchanged. Therefore, if the residence time is increased at x_{ϵ} it must necessarily decrease in other positions. For symmetric distributions, this relationship can be described by the distribution variance. In the absence of noise, a lower variance results in higher reconstructed image quality [19].

In order to explore how RTD variance affects the final time and control effort required, a parametric distribution is considered. The mapping from a parametric distribution to time-dependent trajectories, can enable direct analysis of how parameters affect the trajectory. A Gaussian function with compact support $[x^-, x^+]$, mean x_ϵ and variance δ^2 satisfies the constraints defined above and provides a parameter for variance, making it a good candidate. An example of a Gaussian RTD is given in Figure 3. A Gaussian RTD $\tilde{\tau}_r$ for exposure period τ is given by (11) and (12), where

 $\gamma=(x_{\epsilon}-x^{-})=-(x_{\epsilon}-x^{+})$ and $\tau_{0}=1/\dot{x}(x^{-}).$ The scaling factor A is determined by evaluating the integral in (10).

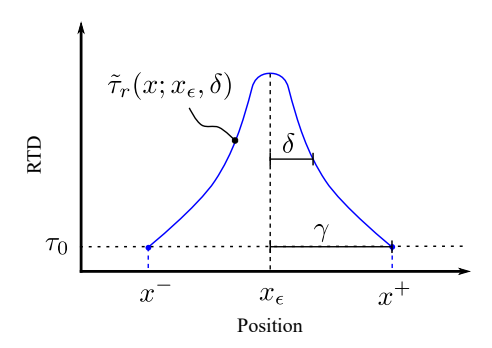


Fig. 3. Conceptual representation of Gaussian RTD.

$$\tilde{\tau}_r(x; x_{\epsilon}, \delta) = A \exp\left[-\frac{(x - x_{\epsilon})^2}{2\delta^2}\right]$$
 (11)

$$A = \tau \sqrt{\frac{1}{2\pi}} \operatorname{erf} \left(\frac{\gamma}{\sqrt{2\delta^2}}\right)^{-1} \tag{12}$$

The dynamics defined by a Gaussian RTD is given by (13). One known solution to ODEs of this form involves the inverse error function [20], as shown in (14).

$$\dot{x}(x) = \frac{1}{A} \exp\left[\frac{(x - x_{\epsilon})^2}{2\delta^2}\right]$$
 (13)

$$x(t) = x_{\epsilon} - \sqrt{2}\delta \operatorname{erfinv}\left(-\sqrt{\frac{2}{\pi}} \frac{t - t_{\epsilon}}{A\delta}\right)$$
 (14)

IV. TRAJECTORY GENERATION

The following initial conditions are given: initial position and time (x_0,t_0) , final position x_f , and exposure duration T_ϵ . Furthermore, the control policy outside of the exposure window is chosen such that it generates constant velocity trajectories. This choice is arbitrary and other control policies can be considered, which will provide different boundary conditions (i.e. by changing v_e).

Trajectories are generated by observing the fact that an entry velocity constraint can only be satisfied for a unique pair (γ, δ) . For the results presented here, the traveled distance γ and entry velocity v_e is considered to be given and the variance parameter δ is numerically determined to satisfy these constraints.

V. RESULTS

A. Simulation Results

Given a travel distance of $\gamma=3$ mm, various entry velocities are considered ($v_e=\{25$ mm/s, 50mm/s, 100mm/s) which result in different δ values. RTDs, trajectories, and exposure velocity profiles are presented in Figures 4, 5, and 6 respectively. Higher entry velocities v_e result in lower final times t_f and are achieved by inverse error trajectories with lower variance δ , but at the cost of higher control effort.

The control effort E for each of the exposure trajectories is evaluated as the ℓ_2 norm of acceleration, as shown in (15). As the variance δ decreases control effort increases as shown in Figure 7, note that control effort is on a logarithmic scale. Additional parameters used for simulation and experimental results are presented in Table I.

$$E = \sqrt{\int_{T_{\epsilon}} \ddot{x}(t)^2 dt}$$
 (15)

 $\label{table I} \textbf{TABLE I}$ Parameters for simulation and experimental results.

x_0	x_f	x_{ϵ}	t_0	au
0 mm	120 mm	60 mm	0 s	0.5 s

In order to verify that inverse error trajectories produce reconstructed images with lower MSE values in comparison to linear and parabolic trajectories, simulation results are generated for various γ and v_e values. For both parameter ranges a set of 30 images are blurred with the expected PSFs, and then reconstructed using Richardson-Lucy deconvolution. Table II presents the MSE values averaged over 30 images for various entry velocities. Table III presents the MSE values averaged over 30 images for various traveled distances.

The robustness of inverse error trajectories to additive Gaussian noise is verified through comparison of MSE values at various noise levels. The linear case is omitted as it is clear that it performs worse than the others, instead the difference between the MSE values of parabolic and inverse error trajectories is presented in Table IV. It should be noted that the error values for inverse error were lower in almost all individual cases for each parameter range. Furthermore, t-tests conducted for the various noise levels demonstrate that the difference in average MSE values is statistically significant when compared to the noise-free case ($\sigma=0$) with a confidence level of at least 95%.

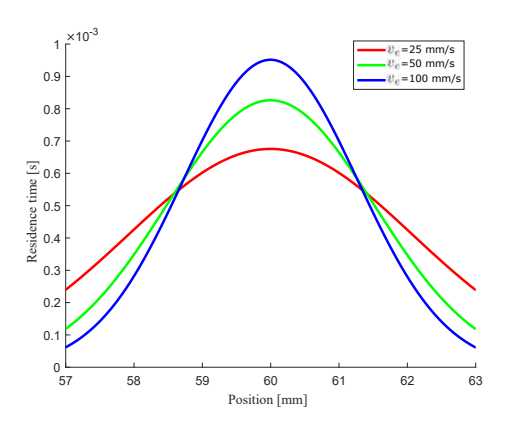


Fig. 4. Residence time distribution for varying v_e .

B. Experimental Setup

An experimental set-up, shown in Figure 8, is used to generate motion blurred images under different trajectories.

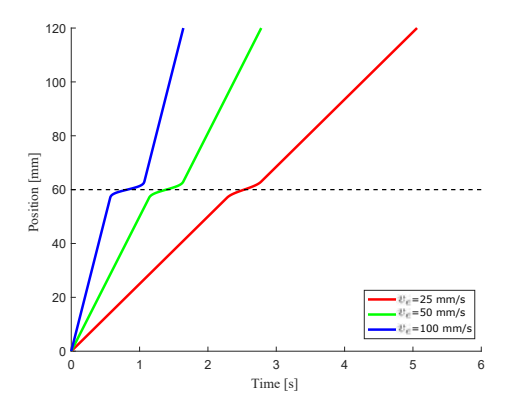


Fig. 5. Trajectories for varying v_e .

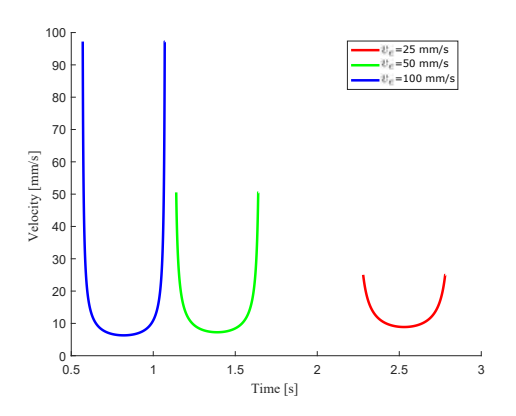


Fig. 6. Velocity profiles of exposure trajectories for varying v_e .

TABLE II $\label{eq:Average MSE} \text{Average MSE of reconstructed images for various entry } \\ \text{velocities with } \gamma = 3 \text{ mm and } \sigma = 0.002.$

v_e	Linear	Parabolic	Inverse Error
25 mm/s	1.891E-2	1.807E-2	1.601E-2
50 mm/s	1.891E-2	1.727E-2	1.362E-2
100 mm/s	1.890E-2	1.685E-2	1.246E-2

A miniature camera with global shutter (model XiC, 2.3 MP CMOS, Ximea Co.) is used with an exposure time $\tau=0.5~\rm s$. A longer exposure time is used in order to simulate the effects of a fast-moving camera, while actually moving at

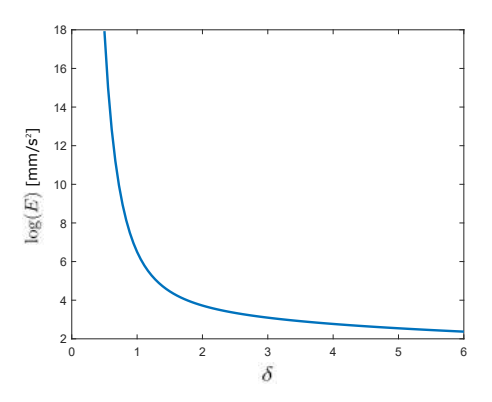


Fig. 7. Relationship between δ and E for $\gamma=3$ mm.

TABLE III

Average MSE of reconstructed images for various traveled distances with $v_e=50$ mm/s and $\sigma=0.002$.

v_e	Linear	Parabolic	Inverse Error
2 mm	1.725E-2	1.551E-2	1.073E-2
3 mm	1.892E-2	1.724E-2	1.353E-2
5 mm	1.725E-2	1.551E-2	1.073E-2

TABLE IV

Average MSE of reconstructed images for various noise variance values with $\gamma=3$ mm, and $v_e=50$ mm/s.

σ	Parabolic	Inverse Error	Difference
0	1.491E-2	1.256E-2	2.346E-3
0.001	3.779E-2	2.462E-2	1.328E-2
0.005	3.779E-2E-2	2.462E-2	1.328E-2
0.01	2.501E-2	1.800E-2	7.054E-3
0.05	1.299E-1	7.160E-3	5.890E-2

moderate speeds (30-70 mm/s). The camera is translated along one dimension on a linear stage that is actuated by a NEMA-23 stepper motor. Commands are generated on a computer and sent through a stepper motor controller (model STR4, Applied Motion Products).

C. Experimental Results

Three trajectories are compared that result in the same final time t_f : (i) linear, (ii) parabolic, and (iii) inverse error. These trajectories are shown in Figure 9. It should be noted that the parabolic trajectory being used here is not the same as the one used in [11], which would not satisfy the objective of reaching position x_f . Instead two parabolic curves have been composed to generate a trajectory that is a path from x_0 to x_f .

The blurry images generated under the various trajectories are presented in Figure 10. MSE values and control effort required, shown in Table V, are evaluated for each trajectory. The static image is used as a reference for MSE calculations. The results show that while greater effort is required for inverse error trajectories in comparison to parabolic trajectories, a lower MSE value is achieved.

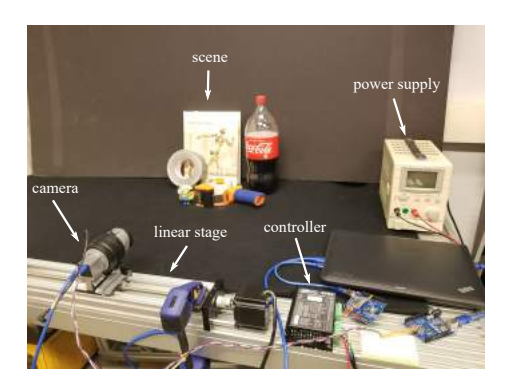


Fig. 8. Experimental setup for capturing motion blurred images with different trajectories.

TABLE V ${\rm RMS\ errors\ }(e_{RMS})\ {\rm and\ control\ effort\ }(E)\ {\rm for\ various\ }$ ${\rm trajectories.}$

	Linear	Parabolic	Inverse Error
MSE	1.594E-2	1.038E-2	8.009E-3
$E \left[\text{mm/s}^2 \right]$	0	2.758E5	7.507E8

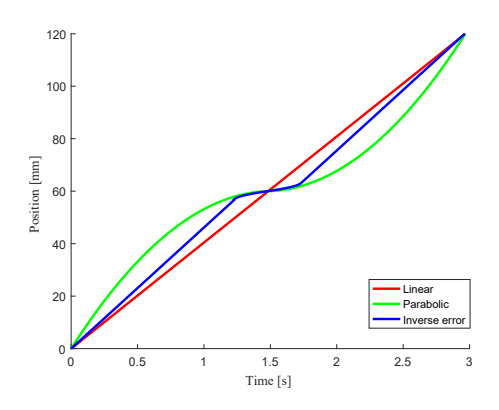


Fig. 9. Trajectories used for experimental setup.

VI. CONCLUSION

This work has two main contributions: (i) residence time analysis, and (ii) inverse error function trajectories. The use of RTDs for motion blur analysis, to the authors' best knowledge, has not been presented in prior literature. This analytical tool provides a mapping between camera trajectories and the expected PSF, through velocity information. Inverse error trajectories are shown to be one solution for generating Gaussian PSFs. RTDs with lower variance result in trajectories with lower final times, at the cost of higher control effort. Experimental results provide verification of the simulation results, which demonstrate that inverse error trajectories result in lower MSE when compared to linear and parabolic trajectories.

While several arguments have been made for why Gaussian RTDs are good candidates for generating trajectories, other RTDs can be considered as well. However, the usefulness of Gaussian RTDs extends beyond their mathematical utility; characteristics such as minimum group delay make Gaussian filters ideal time-domain filters [21]. More work needs to be done to further characterize the motion blur effects of Gaussian RTDs, create a general framework for inverse error trajectory generation (position and orientation), and provide experimental validation on faster moving systems.

REFERENCES

- [1] B. Horn, Robot vision. MIT press, 1986.
- [2] D. Burr, "Motion smear," Nature, vol. 284, no. 5752, p. 164, 1980.
- [3] R. Raskar, A. Agrawal, and J. Tumblin, "Coded exposure photography: motion deblurring using fluttered shutter," ACM Transactions on Graphics (TOG), vol. 25, no. 3, pp. 795–804, 2006.
- [4] E. E. Fenimore and T. M. Cannon, "Coded aperture imaging with uniformly redundant arrays," *Appl. Opt.*, vol. 17, no. 3, pp. 337–347, Feb 1978.

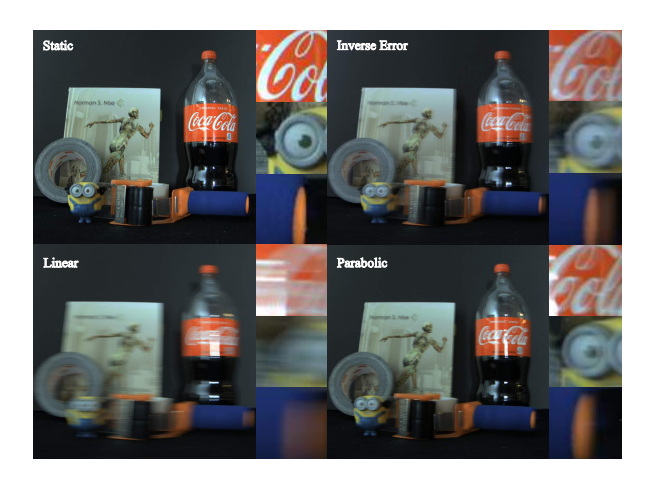


Fig. 10. Blurry images captured under various trajectories.

- [5] D. Znamenskiy, H. Schmeitz, and R. Muijs, "Motion invariant imaging by means of focal sweep," in 2011 IEEE International Conference on Consumer Electronics (ICCE), Jan 2011, pp. 91–92.
- [6] S. K. Nayar and M. Ben-Ezra, "Motion-based motion deblurring," IEEE Trans. Pattern Anal. Mach. Intell., vol. 26, no. 6, pp. 689–698, 2004.
- [7] R. Fergus, B. Singh, A. Hertzmann, S. T. Roweis, and W. T. Freeman, "Removing camera shake from a single photograph," in ACM Transactions on Graphics (TOG), vol. 25, no. 3. ACM, 2006, pp. 787–794.
- [8] Q. Shan, J. Jia, and A. Agarwala, "High-quality motion deblurring from a single image," in ACM Transactions on Graphics (TOG), vol. 27, no. 3. ACM, 2008, p. 73.
- [9] S. Cho and S. Lee, "Fast motion deblurring," in ACM Transactions on Graphics (TOG), vol. 28, no. 5. ACM, 2009, p. 145.
- [10] A. Levin, P. Sand, T. S. Cho, F. Durand, and W. T. Freeman, "Motion-invariant photography," in ACM Transactions on Graphics (TOG), vol. 27, no. 3. ACM, 2008, p. 71.
- [11] T. S. Cho, A. Levin, F. Durand, and W. T. Freeman, "Motion blur removal with orthogonal parabolic exposures," in *Computational Photography (ICCP)*, 2010 IEEE International Conference on. IEEE, 2010, pp. 1–8.
- [12] Y. Bando, B.-Y. Chen, and T. Nishita, "Motion deblurring from a single image using circular sensor motion," in *Computer Graphics Forum*, vol. 30, no. 7. Wiley Online Library, 2011, pp. 1869–1878.
- [13] G. Boracchi and A. Foi, "Modeling the performance of image restoration from motion blur," *IEEE Transactions on Image Processing*, vol. 21, no. 8, pp. 3502–3517, 2012.
- [14] K. Mitra, O. S. Cossairt, and A. Veeraraghavan, "A framework for analysis of computational imaging systems: Role of signal prior, sensor noise and multiplexing," *IEEE Trans. Pattern Anal. Mach. Intell.*, vol. 36, no. 10, pp. 1909–1921, Oct 2014.
- [15] M. D. Kim and J. Ueda, "Dynamics-based motion deblurring for a biologically-inspired camera positioning mechanism," in *Intelligent Robots and Systems (IROS)*, 2013 IEEE/RSJ International Conference on. IEEE, 2013, pp. 2689–2694.
- [16] ——, "Real-time panoramic image generation and motion deblurring by using dynamics-based robotic vision," *IEEE/ASME Transactions* on *Mechatronics*, vol. 21, no. 3, pp. 1376–1387, 2016.
- [17] W. H. Richardson, "Bayesian-based iterative method of image restoration," *JOSA*, vol. 62, no. 1, pp. 55–59, 1972.
- [18] D. Fish, J. Walker, A. Brinicombe, and E. Pike, "Blind deconvolution by means of the richardson–lucy algorithm," *JOSA A*, vol. 12, no. 1, pp. 58–65, 1995.
- [19] J. A. O'Sullivan, M. Jiang, X.-m. Ma, and G. Wang, "Axiomatic quantification of multidimensional image resolution," *IEEE Signal Processing Letters*, vol. 9, no. 4, pp. 120–122, 2002.
- [20] A. Strecok, "On the calculation of the inverse of the error function," *Mathematics of Computation*, vol. 22, no. 101, pp. 144–158, 1968.
- [21] H. Blinchikoff and H. Krause, Filtering in the time and frequency domains. The Institution of Engineering and Technology, 2001.